Open Ceramics 9 (2022) 100205

Contents lists available at ScienceDirect

Open Ceramics

journal homepage: www.sciencedirect.com/journal/open-ceramics

Densification of irregular polydispersed glass particles described as a complex relaxation process

J.L. Amorós [a,b], E. Blasco [a,*], C. Feliu [a,b], A. Moreno [a,b]

[a] Instituto de Tecnología Cerámica – Asociación de Investigación de las Industrias Cerámicas, Spain
[b] Department of Chemical Engineering. Universitat Jaume I, Campus Universitario Riu Sec, 12006, Castellon, Spain

ARTICLE INFO

Keywords:
Glass sintering
Kinetic model
Operating variables

ABSTRACT

The sintering of compacts of irregular non-crystallising glass particles was studied by isothermal and constant-rate heating experiments in a hot stage microscope. The resulting data fitted very well to kinetic equations developed in this study, in which sintering is assumed to be a complex relaxation process, described by the Kohlrausch–Williams–Watts (KWW) relaxation function. The effect of compact pressing pressure, heating rate, and particle size distribution on the sintering curve was determined. It was generally verified that the effect of temperature on the sintering rate could be described by the effect of temperature on the inverse of glass viscosity. For industrial particle size distributions, that the pre-exponential factor of the process rate constant (or inverse of relaxation time) increased with pressing pressure and decreased with the inverse of particle mean radius. For abnormally wide particle distributions a combination of KWW functions were required.

1. Introduction

Glass powder sintering is widely used in fabricating sintered glass, sintered glass-ceramics, glass matrix compacts, and glazes [1–5].

Glass sintering kinetics has been modelled, usually assuming an idealised homogeneous microstructure. Indeed, to describe compact densification, in initial stage sintering Frenkel [6] assumes a regular packing of spherical particles of the same size, r, and in the final stage of sintering, Mackenzie–Shuttleworth (MS) [7] assume porous compacts having spherical pores of the same radius, a. The Frenkel model [6] predicts a sintering rate directly proportional to glass surface tension, γ, and inversely proportional to glass viscosity, η, and to particle radius, r. The group (rη/γ) is also known as capillary relaxation time [8]. This model is not fully consistent with the experiment data and finite element simulations [9–11]. The MS model leads to an expression of the type:

$$\frac{d\rho}{dt} = \frac{3\gamma}{2a\eta}(1-\rho) \qquad \text{Eq. 1}$$

where pore radius, a, decreases as compact relative density, ρ, increases. Generally, in Eq. (1), a is usually replaced with initial pore radius, a_0, [12,13]. With this simplification, Eq. (1) can be readily integrated to yield equation:

$$\frac{1-\rho}{1-\rho_0} = \frac{\varepsilon}{\varepsilon_0} = exp\left(-\frac{3\gamma}{2a_0\eta}t\right) \qquad \text{Eq. 2}$$

or:

$$\frac{\varepsilon}{\varepsilon_0} = exp\left(-\frac{3}{2}\frac{t}{\tau_b}\right) \qquad \text{Eq. 3}$$

where ε and ε_0 are instantaneous and initial porosity, respectively, and $\tau_b = a_0\eta/\gamma$. This model is known as the exponential model [8], and τ_b as bubble relaxation time [8].

The MS and exponential models were verified to be acceptable except for low porosities [8], though the exponential model fitted better to the data than the MS model. This discrepancy is fundamentally due to the presence of occluded gases in the closed pores. The presence of gases in pores, which leads to a minimum residual porosity, has been widely confirmed by experiments [8,13–15].

The cluster model [13], used for monomodal particle size distributions, assumes that: "*small particles preferentially cluster in the open spaces left by larger particles and sinter faster*". Thus, for this model, compact total shrinkage is the weighted sum of the shrinkage due to each size fraction into which the distribution can be divided, any interaction between differently sized particles being disregarded. Nor is this model appropriate for low porosities.

* Corresponding author.
E-mail address: encarna.blasco@itc.uji.es (E. Blasco).

https://doi.org/10.1016/j.oceram.2021.100205
Received 8 September 2021; Received in revised form 1 December 2021; Accepted 3 December 2021
Available online 10 December 2021

Glass particles prepared by traditional methods, such as crushing or milling, are irregular. In these cases, the initial stage sintering rate is faster than that predicted by the Frenkel model [6], as these particles exhibit a shorter capillary relaxation time owing to the much smaller curvature radius of irregular particles than the particle equivalent radius (mean radius). In final stage sintering, the inappropriateness of these models is essentially due to the presence of gases occluded in the pores. On the other hand, the exponential model was verified to describe the sintering process well, except at high degrees of densification.

In the continuum mechanics of sintering [16,17], in absence of stresses (i.e. free sintering), the densification rate or macroscopic strain rate, $d\rho/\rho dt$, is proportional to sintering stress, P_L, and is inversely proportional to bulk viscosity, K_p. P_L represents the collective action of all capillary stresses in the porous material, and K_p represents the viscous resistance to densification. The Skorohod–Olevsky Viscous Sintering (SOVS) model [17,18] defines a dimensionless bulk viscosity, $\psi(\rho)$, which is solely a function of relative density and a dimensionless sintering stress, $\wp(\rho)$, also exclusively a function of ρ, such that the densification rate becomes:

$$\frac{d\rho}{\rho dt} = \frac{3}{2}\frac{\gamma}{r\eta}\frac{\wp(\rho)}{\psi(\rho)} \quad \text{Eq. 4}$$

or:

$$\frac{d\rho}{\rho dt} = \frac{3}{2}\frac{1}{\tau_S}\frac{\wp(\rho)}{\psi(\rho)} \quad \text{Eq. 5}$$

The sintering rate is therefore inversely proportional to a sintering relaxation time, $\tau_S = r\eta/\gamma$, and proportional to a dimensionless function of ρ, the ratio $\wp(\rho)/\psi(\rho)$. To determine $\psi(\rho)$, empirical expressions [19,20], theoretical expressions [18,21,22], or semi-empirical expressions [23] that describe the effect of ρ on porous glass viscosity are used. In contrast, to determine the function $\wp(\rho)$, the authors generally consider different ideal porous structures, which yield expressions of sintering stress, $\wp(\rho)$ [18,21,23]. For spherical particles of the same size, Skorohold [17,18] obtains an equation analogous to Eq. (2):

$$\frac{\varepsilon}{\varepsilon_0} = exp\left(-\frac{9}{4}\frac{\gamma}{r\eta}t\right) \quad \text{Eq. 6}$$

However, the evolution with densification of pore structure shape and form, either open or closed, is so complex that it is virtually impossible to deduce a function that actually describes the relationship between dimensionless sintering stress and relative density, $\wp(\rho)$, including in packings of spherical particles of the same size [14,24], particularly when porosity is exclusively closed.

Thus, no theoretical models are currently available that can accurately describe glass particle sintering or take into account the effect of certain operating variables and/or powder characteristics (compaction pressure, heating rate, particle size distribution, etc.) on this process. Taking into account the generic definition of the relaxation process as the change from one physical state to another involving the dissipation of energy [25], and that the Kohlrausch–Williams–Watts (KWW) relaxation function [26–28] describes complex relaxation processes as the weighted sum of a series of simpler systems, the present study examines the suitability of this function for describing the glass particle sintering process, considering it to be a complex relaxation process. To do so, first, the function's validity both in isothermal sintering and in constant-rate heating was verified. The effect of particle size distribution, compact pressing pressure, and heating rate on the parameters of the KWW function was also studied. The influence of these microstructural characteristics on the KWW function parameters was interpreted in terms of how these characteristics affected relaxation time distribution.

1.1. Glass particle sintering: a complex relaxation process

Glass particle sintering is an irreversible process, in which an initially very porous material – therefore having high surface energy – evolves as the process progresses, decreasing the material's specific surface area and porosity and increasing its shrinkage to a maximum value (minimum porosity) when the system reaches equilibrium, which is generally metastable. Generally, in this state, the pressure of the gases occluded in the pores equals sintering pressure. Prolonged heat treatment leads to lower shrinkage and higher porosity. Only when sintering occurs under vacuum does the system's state of equilibrium coincide with suppression of porosity.

In terms of non-equilibrium thermodynamics, the rate of progress of any irreversible process can be described by the De Donder equation [29–31]:

$$\frac{d\zeta}{dt} = -\frac{1}{\tau^*(T)}(\zeta - \zeta_{eq}) \quad \text{Eq. 7}$$

where ζ is the material's property or characteristic being considered and τ* is relaxation time.

Separating variables and integrating between the initial condition: $t = 0 \rightarrow \zeta = \zeta_0$ and the generic condition: $t = t \rightarrow \zeta = \zeta$ yields an expression that relates the degree of process progress, X, to time:

$$X = \frac{\zeta - \zeta_{eq}}{\zeta_0 - \zeta_{eq}} = exp\left(-\frac{t}{\tau^*}\right) \quad \text{Eq. 8}$$

Applying Eq. (8), which is of a general character, to the particular case of the sintering of compacts of spherical and identical glass particles and assuming the structural characteristic, ζ, to be the porosity of the compact, ε, one obtains:

$$X = \frac{\varepsilon - \varepsilon_{eq}}{\varepsilon_0 - \varepsilon_{eq}} = exp\left(-\frac{t}{\tau^*}\right) \quad \text{Eq. 9}$$

This equation, for $\varepsilon \gg \varepsilon_{eq}$ or $\varepsilon_{eq} \approx 0$, becomes the Eq. (6). For this model, $\tau^* = (4/9)(r\eta/\gamma)$ or $\tau^* = (4/9)\,\tau_S$. Porosity at equilibrium is the minimum value reached by the compact, $\varepsilon_{eq} = \varepsilon_{min}$, which depends, among other variables, on kiln atmosphere and on porosity and pore size when the compact seals.

However, in real irregular glass particle packings, particle size and curvature radius, interparticle contacts, and pore size and shape are not homogeneous either at sintering start or during sintering progress. Therefore, this real, heterogeneous and complex material may be assumed, at least conceptually, to be made up of simpler systems, involving very small and intrinsically homogeneous structural units having different structural characteristics from each other. Each of these microregions may therefore be assumed to exhibit a sintering or relaxation process, described by Eq. (9), but with a different relaxation time, τ_i. The overall sintering process of the entire compact may thus be assumed to be the weighted sum of a series of "n" simple relaxation processes, each having a different relaxation time, τ_i, depending on its microstructure (number and nature of interparticle contacts, particle and pore size and distribution, etc.). Consequently, assuming a continuous distribution of relaxation time, τ_i, one obtains:

$$X = \sum_{i=1}^{i=n} exp\left(-\frac{t}{\tau_i}\right) = \int_0^\infty \rho(\tau_i) exp\left(-\frac{t}{\tau_i}\right) d\tau_i \quad \text{Eq. 10}$$

where $\rho(\tau_i)$ is the relaxation time distribution function of each individual process. It has been shown [27,28] that Eq. (10) is numerically equal to the Kohlrausch–Williams–Watts (KWW) relaxation function or stretched exponential function:

$$X = exp\left[-\left(\frac{t}{\bar{\tau}}\right)^m\right] \quad \text{Eq. 11}$$

It has also been verified that, the wider the distributions $\rho(\tau_i)$, the smaller are the values of parameter m (Fig. 1), albeit always: $0 < m \leq 1$ [26–28].

Eq. (11) therefore describes the overall sintering process, where $\bar{\tau}$ is a

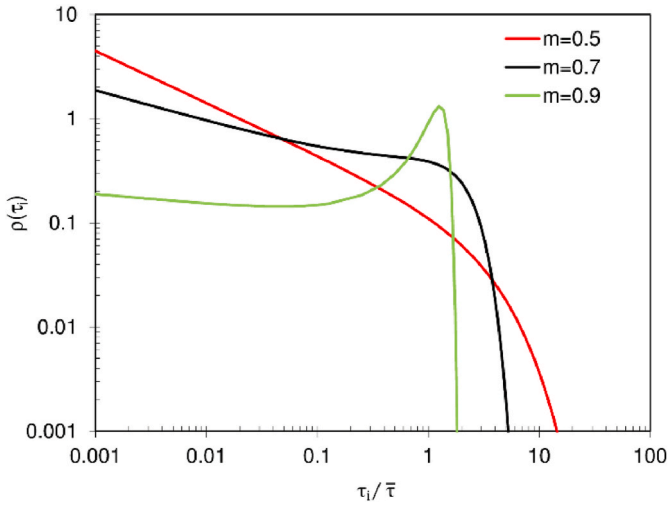

Fig. 1. Plot of the probability density function, $\rho(\tau_i)$, as a function of dimensionless relaxation time, $\tau_i/\bar{\tau}$, for values of stretching parameter m = 0.5, m = 0.7, and m = 0.9 [26].

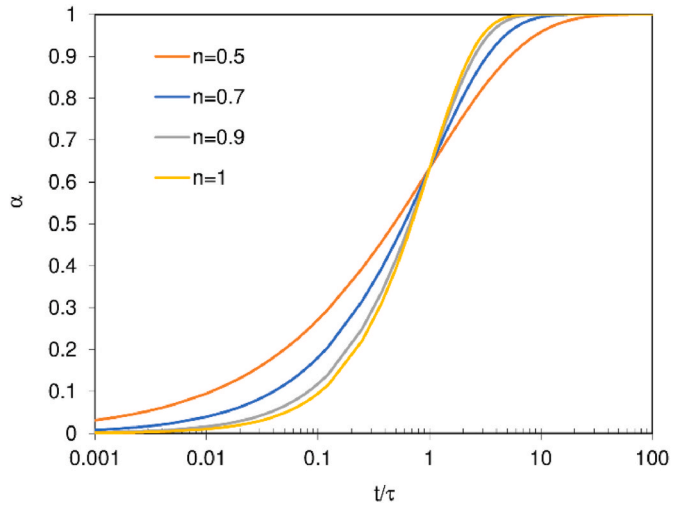

Fig. 2. Evolution of sintering progress, α, with dimensionless sintering time, t/τ, for different values of n (Eq. (16)).

mean relaxation time that depends on the distribution of its individual values, $\rho(\tau_i)$, which in turn depends on the number and nature of these different microregions, i.e. on the microstructural heterogeneity of the green compact.

For the sintering of glass particle compacts, Eq. (11) may be expressed in the form:

$$X = \frac{\varepsilon - \varepsilon_{min}}{\varepsilon_0 - \varepsilon_{min}} = \frac{\rho_{max} - \rho}{\rho_{max} - \rho_0} = exp\left[- \left(\frac{t}{\bar{\tau}}\right)^n \right] \quad \text{Eq. 12}$$

since $\varepsilon_i = 1 - \rho_i$.

With a view to relating the degree of sintering progress, α, to a readily measurable magnitude such as compact volume, V, or cylinder silhouette area, S, the second term in Eq. (12) will be mathematically manipulated. Thus, adding unity to the first term and subtracting the fraction $(\rho_{max} - \rho)/(\rho_{max} - \rho_0)$ results:

$$\alpha = \frac{\rho - \rho_0}{\rho_{max} - \rho_0} = 1 - exp\left[- \left(\frac{t}{\tau}\right)^n \right] \quad \text{Eq. 13}$$

Operating, one yields:

$$\alpha = \frac{1 - \frac{\rho}{\rho_0}}{1 - \frac{\rho_{max}}{\rho_0}} = 1 - exp\left[- \left(\frac{t}{\tau}\right)^n \right] \quad \text{Eq. 14}$$

Considering the approximation for the series of natural logarithms:

$$1 - y \approx ln\frac{1}{y} \quad for \;\; y < 2 \quad \text{Eq. 15}$$

The Eq. (14) becomes:

$$\alpha = \frac{ln\frac{\rho_0}{\rho}}{ln\frac{\rho_0}{\rho_{max}}} = \frac{ln\frac{V}{V_0}}{ln\frac{V_{min}}{V_0}} = \frac{\varepsilon_V}{\varepsilon_{V,max}} = 1 - exp\left[- \left(\frac{t}{\tau}\right)^n \right] \quad \text{Eq. 16}$$

where V, V_0 and V_{min} are the initial, instantaneous, and minimum volume of the test pieces, and ε_V is the volume strain.

1.1.1. *Isothermal sintering. Kinetic equation*

Eq. (16) relates the degree of sintering progress, α, to dimensionless time, t/τ, and to the stretching parameter, n, (Fig. 2).

The amplitude of the sintering range, defined as the difference between the dimensionless time required to reach virtually full densification and process onset, increased as n decreased, in accordance with the relaxation time distribution function (Fig. 1). In addition, for dimensionless time t/τ = 1, the degree of sintering progress was α = 0.63, regardless of the value of n: in other words, relaxation time was the time required for sintering to reach a degree of progress of α = 0.63.

Rearranging Eq. (16) yields the expression:

$$\frac{t}{\tau} = g(\alpha) = \left[- ln(1 - \alpha) \right]^{\frac{1}{n}} \quad \text{Eq. 17}$$

where g(α) is the integrated form of the kinetic model, with a stretching parameter value of $0 \leq n \leq 1$.

Analogously, the kinetic model of sintering, in differential form, becomes:

$$f(\alpha) = n(1 - \alpha)\left[- ln(1 - \alpha) \right]^{\frac{n-1}{n}} \quad \text{Eq. 18}$$

and the process rate:

$$\frac{d\alpha}{dt} = \frac{1}{\tau} f(\alpha) = \frac{1}{\tau} n(1 - \alpha)\left[- ln(1 - \alpha) \right]^{\frac{n-1}{n}} \quad \text{Eq. 19}$$

The kinetic model in differential form, f(α) (Eq. (18)), exclusively describes the dependence of process rate on the degree of sintering progress. Indeed, the relationship between the instantaneous rate of the process and the rate corresponding to a degree of advance of α = 0.5, $[d\alpha/dt]/[d\alpha/dt]_{\alpha = 0.5}$, is dimensionless and, in accordance with Eq. (19), independent of thermal treatment and equal to f(α)/f(0.5), that is, to the relationship between the value of the instantaneous kinetic model and that corresponding to α = 0.5. The dimensionless rate of sintering, $[d\alpha/dt]/[d\alpha/dt]_{\alpha = 0.5} = f(\alpha)/f(0.5)$, for a given material is therefore only a function of parameter n. Plotting the values of the dimensionless rate against process progress, for different values of n, reveals the effect of the stretching parameter on the decrease in the dimensionless rate of sintering with process progress (Fig. 3). Indeed, for $\alpha \leq 0.5$, the dimensionless rate of sintering and its decrease with process progress (slope of these curves) increased as n decreased, particularly at sintering onset ($\alpha \approx 0$). In contrast, for $\alpha \geq 0.5$, as n decreased, the dimensionless rate of sintering decreased and the rate at which it did so (curve slope) increased, particularly at the end of sintering ($\alpha \approx 1$).

1.1.2. *Non-isothermal sintering. Kinetic equation*

According to Eq. (19), sintering process kinetics can be described as:

$$\frac{d\alpha}{dt} = \tau^{-1}(T) f(\alpha) \quad \text{Eq. 20}$$

In previous studies, the effect of temperature on the constant rate of the process, $\tau^{-1}(T)$, was verified to be the same as the effect on the inverse of glass matrix viscosity [3,4,32], the latter being described by the

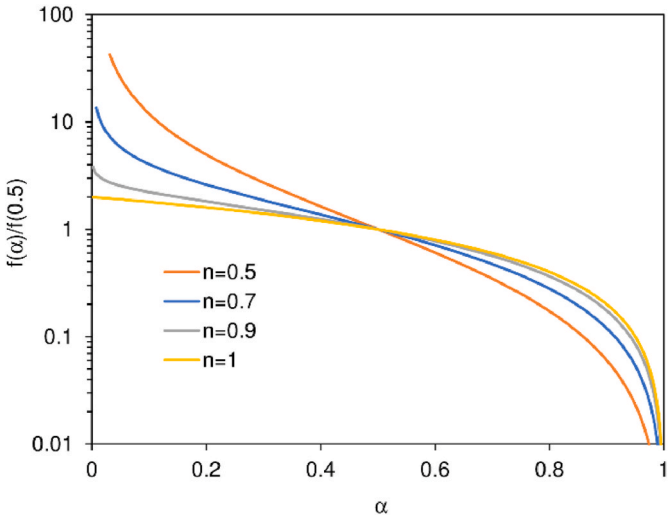

Fig. 3. Evolution of the dimensionless rate of sintering, $[d\alpha/dt]/[d\alpha/dt]_{\alpha=0.5} = f(\alpha)/f(0.5)$, with the degree of sintering progress, α, for different values of n.

Vogel–Fulcher–Tammann (VFT) equation:

$$\eta = \eta_0 exp\left(\frac{B}{T - T_{VFT}}\right) \quad \text{Eq. 21}$$

where B, T_{VFT}, and η_0 are the values of the VFT equation parameters.

Thus:

$$\tau^{-1}(T) = A exp\left(-\frac{B}{T - T_{VFT}}\right) \quad \text{Eq. 22}$$

where A is a pre-exponential factor proportional to γ/η_0 and, in principle, also proportional to the inverse of particle mean radius, that is: $A \propto \gamma/r\eta_0$. However, this parameter may also be influenced by other microstructural characteristics and operating variables.

If the process develops at constant-rate heating, β, Eq. (20) and Eq. (22) yield:

$$\frac{d\alpha}{dT} = \frac{A}{\beta} exp\left(-\frac{B}{T - T_{VFT}}\right) f(\alpha) \quad \text{Eq. 23}$$

Separating variables and integrating one obtains the integral form of the kinetic model, g(α), and its relation to temperature. Using the Murray and White approximation [33] yields:

$$g(\alpha) = \int_0^{\alpha} \frac{d\alpha}{f(\alpha)} = \frac{A}{\beta} \int_0^{T} exp\left(-\frac{B}{T - T_{VFT}}\right) dT = \frac{AR(T - T_{VFT})^2}{\beta B} exp\left(-\frac{B}{T - T_{VFT}}\right) \quad \text{Eq. 24}$$

Replacing g(α) with Eq. (17) in Eq. (24) and rearranging terms one obtains:

$$\alpha = 1 - exp\left\{-\left[\left(\frac{A}{\beta}\right)\left(\frac{(T - T_{VFT})^2}{B}\right) exp\left(-\frac{B}{T - T_{VFT}}\right)\right]^n\right\} \quad \text{Eq. 25}$$

1.1.3. The Ozawa method

Rearranging terms in Eq. (25) and taking logarithms yields:

$$ln[-ln(1-\alpha)] = nln\left(\frac{A(T - T_{VFT})^2}{\beta B}\right) - \frac{nB}{T - T_{VFT}} \quad \text{Eq. 26}$$

Based on Eq. (26), for experiments at different heating rates, β, plotting the pair of values $(\alpha, \beta)_T$ corresponding to the same temperature, in the form $ln[-ln(1-\alpha)]$ versus lnβ, yields a straight line of slope -n [34]. That is:

$$\left.\frac{\partial[ln(-ln(1-\alpha))]}{\partial ln\beta}\right|_T = -n \quad \text{Eq. 27}$$

2. Materials and experimental procedure

A borosilicate frit of composition (Table 1) close to that of glass SRM 717a [35], used as reference material for determining the viscosity–temperature curve, was obtained by dry mixing appropriate amounts of quartz, boric acid, potassium carbonate, alumina, sodium carbonate, and lithium carbonate. The mixture was fused in an alumina crucible at 1550°C for 30min. The resulting melt was quenched in water, yielding a transparent and homogeneous frit.

The frit particles were wet milled for 30min in an alumina ball mill until particle size distribution (PSD) M was obtained. Frit particle suspension M was milled anew in a zirconia bead mill to obtain a finer PSD, F. To obtain a coarser and wider PSD, MC, the frit was dry milled in a ring mill. Finally, to obtain a coarse but narrow PSD, C, powder MC was wet sieved using a sieve with a mesh aperture of 40 μm.

Particle size distributions F, M, and MC were determined with a laser diffraction instrument. The scatter signal was interpreted using the Fraunhofer diffraction pattern. Particle size distribution C was determined by scanning electron microscopy and image analysis. The number of particles measured was about 3500. Particle size distribution was determined using Olympus image analysis software. The area of each particle was selected as a descriptor, the area being the total number of pixels enclosed within the contour of the element under analysis, multiplied by the area of a previously calibrated pixel (Area = number of pixels × area of one pixel). The area of each particle was used to calculate the equivalent circle diameter (diameter of a circle having the same area as the measured body: ECD = $2(area/\pi)^{1/2}$). The four PSD curves fitted satisfactorily to lognormal distributions (Table 2 and Fig. 4). Most glaze PSDs used in industrial practice range from particle size distribution M to F [36]. Particle size distribution C is similar to the PSD used in dry glaze applications. Particle size distribution MC, which was much wider than the others, was chosen to study the effect of this characteristic.

All the powders were made up of jagged glass particles, which exhibited a sharp radius of curvature at the edges, as shown in the SEM micrographs (Fig. 5). Except for powder C, small glass particles were observed to adhere to the largest ones.

Disks, 5 mm in diameter and 3 mm thick, were compacted in a universal testing machine, using powder slightly moistened with PVA solution, at a displacement rate of 2 mm/min to the required pressure. Pressing pressure was P_{comp} = 30 MPa, except in the experiments intended to determine the influence of this variable on sintering. To determine the fixed viscosity points by hot stage microscopy, cylindrical test pieces, 3 mm in diameter and 5 mm high, were used. A hot stage microscope, HSM, with image analysis and data processing software was used. The computer image analysis system continuously recorded the geometry and projected area of the test piece silhouette, S. To determine the sintering kinetics, constant-rate-heating ($0.5 \leq \beta \leq 60$ K/min) and isothermal heat treatments were conducted. In every case, peak firing temperature exceeded the temperature at which the test piece reached maximum compactness. In the isothermal treatments, the test piece was heated at a rate of β = 25K/min to the set treatment temperature. Treatment time exceeded 400min. If the test piece did not reach maximum density during isothermal treatment, this was extended at a heating rate of β = 25K/min to a temperature that was 50°C higher, followed by an additional 60min isothermal treatment.

The sintering curves were determined from the initial, S_0, instantaneous, S, and minimum, S_{min}, silhouette surface areas of the test pieces. Diametral and axial strains were similar until completion of sintering. Once the sintering process had been completed, test piece geometry changed [4]. Assuming isotropic shrinkage, the sintering progress

Table 1
Oxide composition of the frit (% by weight).

SiO_2	Al_2O_3	B_2O_3	Fe_2O_3	CaO	MgO	Na_2O	K_2O	TiO_2	Li_2O
68.3	4.4	16.6	0.05	0.13	0.07	0.91	7.80	0.05	0.66

Table 2
Geometric mean radius, r, and geometric standard deviation, σ, of the lognormal distribution of the four studied powder PSDs.

PSD	F	M	C	MC
r (μm)	0.8	2.7	91	10.6
σ	1.9	2.6	1.7	5.3

Table 3
Values of the parameters and variance, S^2, obtained on fitting the experimental sintering points to Eq. (25) (from fit 1 to 3) and to Eq. (35) (fit 4). Powder M.

Fit	n	ln A·(s^{-1})	S^2
1	0.7 ± 0.015	17.6 ± 0.3	$9.87\cdot10^{-5}$
2	0.7	17.6 ± 0.3	$2.21\cdot10^{-4}$
3	0.7	17.6	$2.05\cdot10^{-3}$
4	0.7	$ln[A_0\cdot(1+k\beta)]$ $A_0 = 3.21\cdot10^7$ s^{-1} κ = 0.022 s/K	$3.39\cdot10^{-4}$

Table 4
Values of the experimental maximum silhouette surface strain, $-\varepsilon_{S,max}$, calculated initial relative density, ρ_0 (Eq. (31)), and parameters and variance, S^2, obtained on fitting the experimental sintering points to Eq. (35).

PSD	$-\varepsilon_{S,max}$	ρ_0	n	$A_0\cdot10^{-7}$(s^{-1})	κ(min/K)	S^2
F	0.51 ± 0.018	0.46 ± 0.013	0.7	13.1	0.024	$4.2\cdot10^{-4}$
M	0.43 ± 0.021	0.51 ± 0.017	0.7	3		
C	0.29 ± 0.016	0.63 ± 0.014	0.58	0.36		

Table 5
Values of the parameters and variance, S^2, obtained on fitting the experimental sintering points to Eq. (39), Eq. (40), and Eq. (41). Powder MC.

Stage	w_i	n_i	$A_{0i}\cdot10^{-7}$(s^{-1})	κ(min/K)	S^2	r (μm)	r_i (μm)
1	0.75	0.7	4.56	0.017	$4.7\cdot10^{-4}$	10.6	2.3
2	0.25	1	0.129				80

parameter, α, was calculated as:

$$\alpha = \frac{\varepsilon_V}{\varepsilon_{V,max}} = \frac{\varepsilon_S}{\varepsilon_{S,max}} = \frac{ln(S/S_0)}{ln(S_{min}/S_0)} \quad \text{Eq. 28}$$

where ε_S and $\varepsilon_{S,max}$ are the instantaneous and maximum silhouette surface strain, respectively.

Maximum bulk density during the tests was calculated from the measurement of the fired test piece dimensions and the height and width values of the test piece recorded during the HSM experiments. Glass true density, determined by a helium pycnometer, was 2.210 ± 0.04 g/cm^3. Glass maximum relative density, ρ_{max}, varied randomly around a mean value, regardless of the thermal treatment and powder particle size distribution. Averaging all values yielded $\rho_{max} = 0.98 \pm 0.02$.

From the definition of densification strain, $\varepsilon_V = \ln(V/V_0)$, operating one obtains:

$$\rho = \rho_0 exp(-\varepsilon_V) \quad \text{Eq. 29}$$

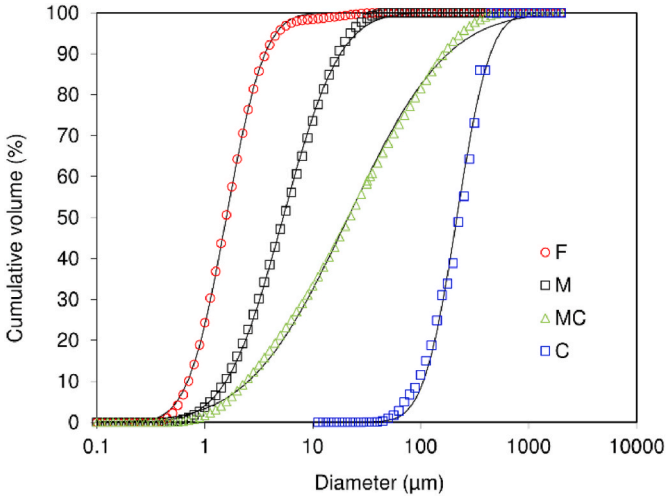

Fig. 4. Particle size distributions of the studied glaze determined by laser diffraction (M, F, and MC) or by SEM and image analysis (C), fitted to the lognormal distribution.

On the other hand, if sintering is isotropic, one obtains:

$$\varepsilon_V = \frac{3}{2}\varepsilon_S \quad \text{Eq. 30}$$

Applying Eq. (29) and Eq. (30) for ρ_{max} and operating yields:

$$\rho_0 = \rho_{max} exp\left(\frac{3}{2}\varepsilon_{S,max}\right) \quad \text{Eq. 31}$$

An expression that allows density at sintering onset to be calculated from the values of ρ_{max} and $\varepsilon_{S,max}$.

3. Results and discussion

3.1. Viscosity curve

The fixed viscosity points obtained experimentally for particle size distribution M, at 10K/min, are detailed in Fig. 6, together with the viscosity values assigned by different authors. The values obtained fitted well to the viscosity–temperature curve given by the National Institute of Standards and Technology [35] for T ≤ 1000°C and described by the Vogel–Fulcher–Tammann equation:

$$log\eta = -3.012 + \frac{5495.3}{T - 148.1} \quad \text{Eq. 32}$$

where η is viscosity expressed in Pa·s and T is temperature in °C.

3.2. Verification of the model

To verify the model, six series of isothermal and constant-rate heating, 0.5≤β≤60 K/min, experiments were conducted, using glass powder of particle size distribution M.

3.2.1. Isothermal sintering

As the test piece had already undergone a certain shrinkage and hence a degree of initial progress, α_0, when the kiln reached the programmed temperature (isothermal treatment start, t = 0), in order to fit

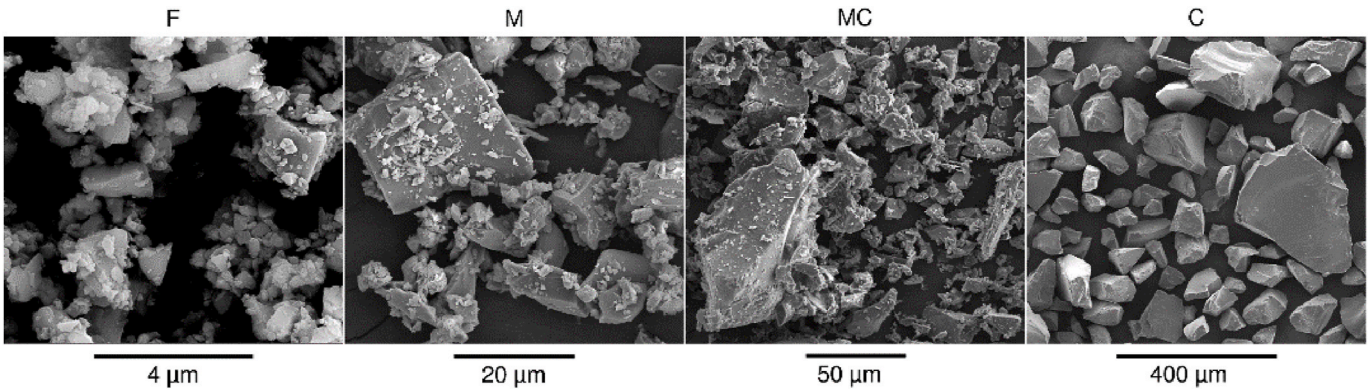

Fig. 5. SEM micrographs of powders F, M, C, and MC.

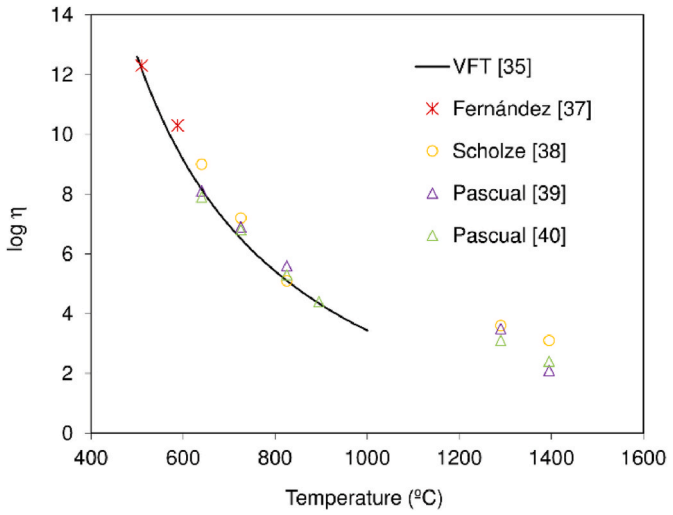

Fig. 6. Characteristic fixed viscosity points according to Fernández [37], Scholze [38], Pascual [39], Pascual [40], and the Vogel–Fulcher–Tammann equation, by SRM 717a [35]. Powder M.

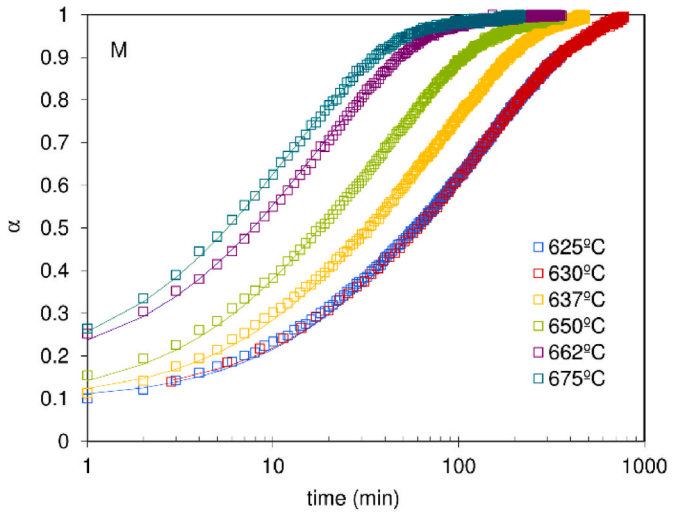

Fig. 7. Isothermal sintering curves. The symbols are experimental data, and the solid lines correspond to the values calculated from the model (Eq. (33) with n = 0.7). Powder M.

the experimental data to the model (Eq. (16) and Eq. (17)) it was necessary to integrate the kinetic equation in differential form (Eq. (19)), taking $t = 0 \rightarrow \alpha = \alpha_0$ as initial condition. The resulting equation was:

$$\alpha = 1 - \frac{1}{exp\left\{\frac{t}{\tau} + \left[-ln(1-\alpha_0)\right]^{1/n}\right\}^n} \qquad \text{Eq. 33}$$

The experimental data corresponding to each temperature were fitted to Eq. (33), first, without fixing any parameter. The values of n were verified to vary very little ($n = 0.7 \pm 0.035$) and to do so randomly. A second fit was therefore made, keeping n constant at 0.7. In every case, the value of S^2 was low (of the order of 10^{-5}). The experimental data and the values calculated in accordance with the second fit are plotted for six different temperatures in Fig. 7. The agreement is observed to be excellent.

For each temperature, sintering relaxation time, $\tau_s = r\,\eta/\gamma$, was calculated from the values of the experimental particle mean radius ($r = 2.66$ µm), from glass surface tension $\gamma = 0.277$ N/m (estimated from the glass composition by the Dietzel equation [37]), and from viscosity at each temperature (calculated from the VFT equation). The values of relaxation time, τ, obtained from the fits versus $\tau_s = r\eta/\gamma$ are plotted in Fig. 8. Both values are observed to be proportional, in accordance with the proposed model.

On plotting the degree of sintering progress, α, versus dimensionless time, t/τ, the results were grouped very well to a single kinetic curve

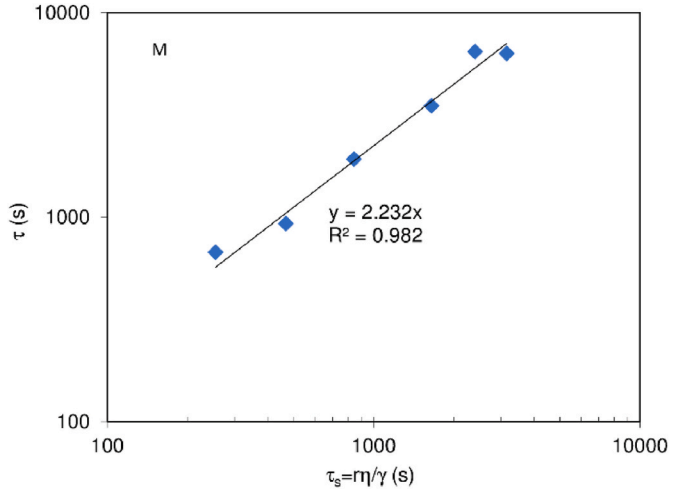

Fig. 8. Comparison of the values of experimental relaxation time, τ, and those of viscous sintering time, $\tau_s = r\eta/\gamma$. Powder M.

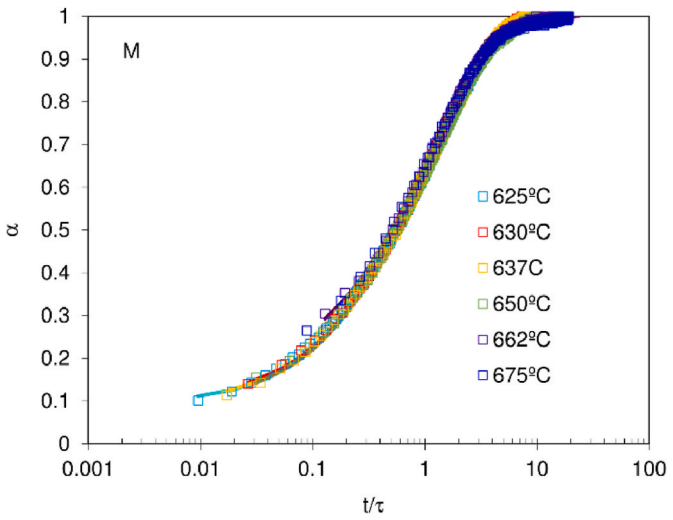

Fig. 9. Evolution of degree of sintering progress, α, with dimensionless time, t/τ, for every test temperature. Powder M.

with n = 0.7 (Fig. 9).

3.2.2. *Non-isothermal sintering*

Six experiments were carried out at constant-rate heating, 0.5≤β≤60 K/min (Fig. 10).

These results were used to estimate the value of n by the Ozawa method (Section 1.1.3). The plot of the values of ln(-ln(1-α)) versus lnβ, for some of the temperatures considered (Fig. 11), yielded straight lines whose slope, -n, oscillated slightly around a mean value: n = 0.65 ± 0.079, which was very close to that obtained by the isothermal method (n = 0.7).

The pairs of experimental values (α, T)$_\beta$ corresponding to each heating rate, β, were fitted to Eq. (25). No fitting parameter was set, first, so that both n and A oscillated around a mean value (fit 1 in Table 3). In fit 2, the value of n was set at 0. 7, and in fit 3 the values of both n and A were set. Obviously, as the number of variable parameters decreased, fit variance increased slightly.

On plotting the curves resulting from fit 3, the experimental curves were observed to depart from the calculated curves in a clear trend according to the heating rate, β. On the other hand, the real rate at which

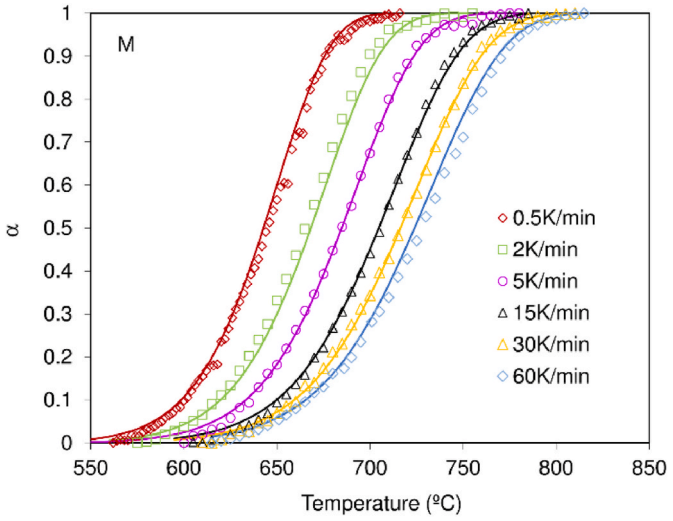

Fig. 10. Non-isothermal sintering curves. The symbols are experimental data, and the solid lines correspond to the values calculated from the model (Eq. (35), fit 4 in Table 3). Powder M.

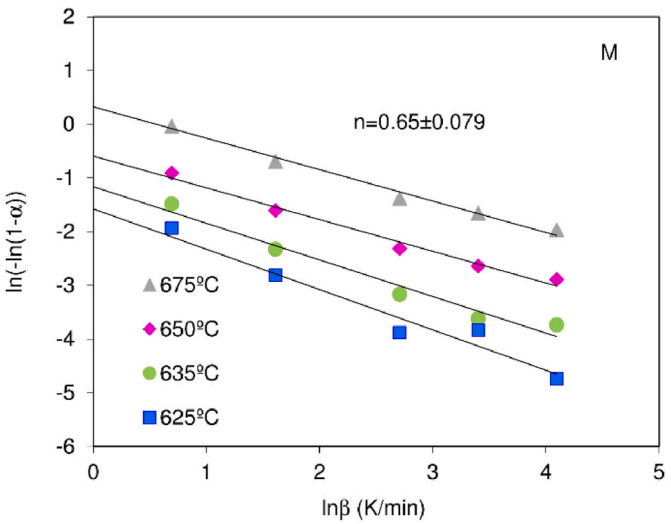

Fig. 11. Ozawa plot for the determination of n. Powder M.

the specimen was heated was always lower than the programmed heating rate, β, and this difference increased as the heating rate, β, rose [41]. To obtain an empirical relationship that corrected this effect, the values of A obtained from fit 2 were plotted versus the heating rate, β (Fig. 12). As already observed in a previous study [5], the results fitted a straight line whose equation was:

$$A = A_0 \cdot (1 + \kappa\beta) \qquad \text{Eq. 34}$$

where κ is a fitting parameter that depends on the thermal properties of the material, test piece size, and kiln configuration and A_0 is the pre-exponential factor when the heating rate tends to zero.

Introducing Eq. (34) into Eq. (25) yields:

$$\alpha = \frac{\varepsilon_S}{\varepsilon_{S,max}} = 1 - exp\left\{ - \left[\frac{A_0 \cdot (1+\kappa\beta)}{\beta} \frac{(T - T_{VFT})^2}{B} exp\left(- \frac{B}{(T - T_{VFT})} \right) \right]^n \right\} \qquad \text{Eq. 35}$$

Using the values of fit 4 in Table 3, the sintering curves were calculated by Eq. (35) (Fig. 10). This model described better than Eq. (25) (albeit appropriate) the influence of the heating rate on the sintering process, using only two empirical fitting parameters: κ and A_0.

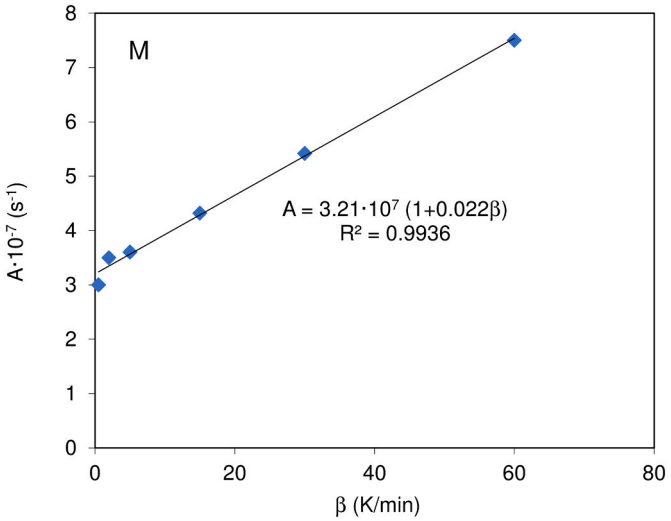

Fig. 12. Variation of the pre-exponential factor, A (Eq. (22)), with heating rate, β. Powder M.

The kiln heating rate, β, in Eq. (25) was replaced with a lower rate (β/(1 + κβ)) in Eq. (35), the latter rate being assumed to be the real rate at which the compact was heated. Thus, A_0 was the pre-exponential factor corresponding to a heating rate that tended to zero. In this case, the temperature at any point in the compact was the same and identical to kiln temperature.

3.2.3. Comparison with other models

To compare the goodness of different models it is very easy and enlightening to calculate, for some of these, the evolution of the dimensionless instantaneous sintering rate with sintering degree of progress.

The curves: dimensionless sintering rate, $(d\alpha/dt)_\alpha/(d\alpha/dt)_{0.5}$, or, f(α)/f(0.5), versus degree of process progress, α, for the relaxation model and for other sintering models were plotted (Fig. 13). In every case, initial relative density was assumed to be $\rho_0 = 0.5$ and $\rho_{max} = 0.98$. The Sura & Panda [20] and Scherer [21] models were calculated from the SOVS model (Eq. (5)), considering the Ducamp & Raj equation [23] for dimensionless sintering stress, $\wp(\rho)$, and considering Sura & Panda's experimental expression [20] and Scherer's theoretically deduced expression [21] for dimensionless bulk viscosity, $\psi(\rho)$. The Sura & Panda model [20] was verified to most closely approximate the relaxation model, which was the model that best described the process.

The developed model further described, for low degrees of sintering progress, higher sintering rates than most of the models. This behaviour reflected the influence of the small curvature radii of irregular particles on the sintering rate. In contrast, for high degrees of sintering progress, the rate described by the developed model was much lower than that predicted by most of the models. This behaviour was related to a progressive increase in closed pores containing occluded gases as the process developed. This phenomenon, which entailed a greater decrease in sintering rate in the final stages of the process, owing to decreased sintering pressure, is not taken into account in the models described in the literature.

3.3. Kinetic equation of non-isothermal viscous sintering. Application to the determination of the effect of some variables on sintering kinetics

Eq. (35) accurately described non-isothermal sintering kinetics with just three fitting parameters: κ, A_0, and n. Parameters B and T_{VFT}, which describe the effect of temperature and glass composition on glass viscosity, can be estimated or experimentally determined. As a result, this equation is suitable for describing the curves: degree of sintering progress versus temperature (sintering curves) in constant-rate heating, β, experiments and the effect of some variables on these curves.

3.3.1. Effect of pressing pressure

Test pieces were formed at six different pressing pressures. Fig. 14 only shows plots of the values of $\varepsilon_S = \ln(S/S_0)$ versus temperature of the test pieces formed at the highest, the intermediate, and the lowest pressing pressure. The absolute value of $-\varepsilon_S$ was observed to increase as compaction pressure decreased, this effect being greater as temperature rose. However, the temperature range in which the test pieces reached maximum densification (750–800°C) or maximum firing shrinkage, $\varepsilon_{A,max}$, was independent of compaction pressure. It was also verified that the values of $-\varepsilon_{S,max}$, though scattered, varied linearly with the logarithm of compaction pressure, P_{comp} (Fig. 15), as has been observed in sintering different types of materials [42,43]. This relationship stems from the increase in relative density at sintering onset, ρ_0 (Eq. (31)), related to $-\varepsilon_{A,max}$, with the logarithm of P_{comp} (Fig. 15).

Introducing $\rho_{max} = 0.98$, which was the mean value obtained of the maximum relative density measurements, and the experimental values of $\varepsilon_{S,max}$ in Eq. (31), the values of ρ_0 were calculated, which are plotted in Fig. 15. Though scattered, the values fitted quite well to a straight line.

Each of the twelve sintering curves, obtained at β = 15K/min using six different pressing pressures, was fitted to Eq. (35) leaving A_0 as sole variable parameter and, for the rest, taking the values of fit 4 in Table 3. In every case, the experimental results fitted very well to the model, as may be verified in Fig. 14. The resulting values of A_0 were observed to increase linearly with green relative density, ρ_0 (Fig. 16). On plotting the values of $-\varepsilon_{A,max}$ versus those of ρ_0 in the same figure (Fig. 16), $-\varepsilon_{A,max}$ was observed to decrease linearly with ρ_0.

The effect of green relative density, ρ_0, on A_0 is described by a linear equation (Fig. 16):

$$A_0 = 16.2 \cdot 10^7 (\rho_0 - 0.335) \quad \text{Eq. 36}$$

Analogously, an increase in pressing pressure raised the value of A_0 and, with it, the sintering rate (Fig. 17). This was because, as pressing pressure rose, green compactness and the number of interparticle contacts increased while pore size decreased.

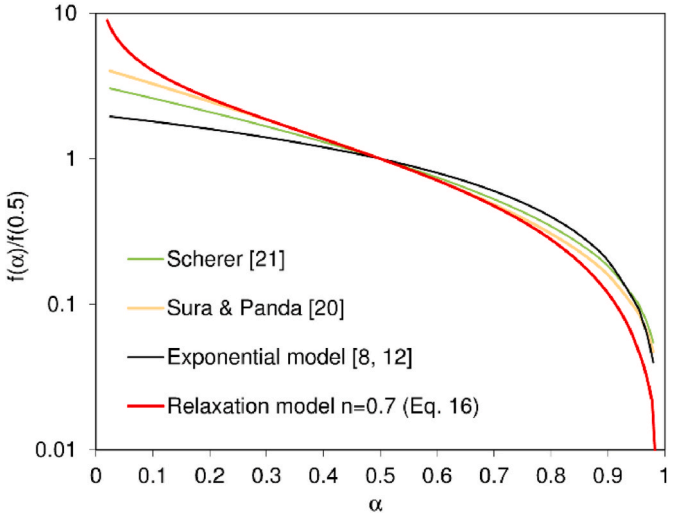

Fig. 13. Evolution of the dimensionless sintering rate, $[d\alpha/dt]/[d\alpha/dt]_{\alpha = 0.5}$ = f(α)/f(0.5), with the degree of sintering progress α, for different models: Scherer [21], Sura & Panda [20], exponential model [8,12], and developed relaxation model (Eq. (16) with n = 0.7).

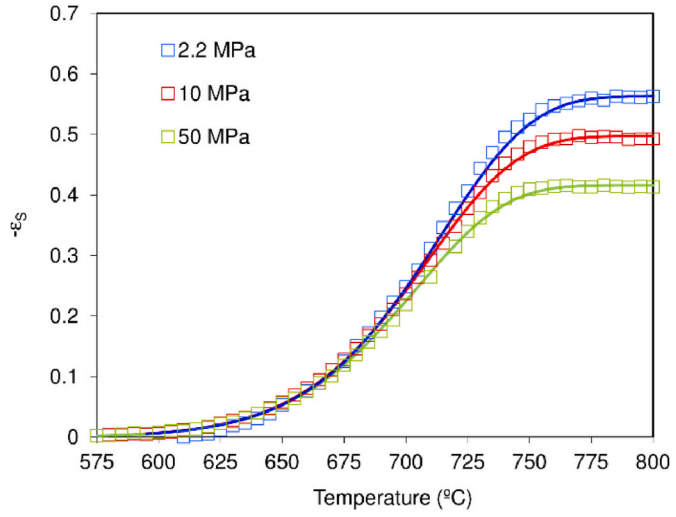

Fig. 14. Evolution of silhouette surface strain, $-\varepsilon_S$, with temperature for P_{comp} = 2.2, 10, and 50 MPa. Powder M and β = 15K/min. The symbols are experimental data, and the solid lines correspond to the values calculated from Eq. (35) with n = 0.7.

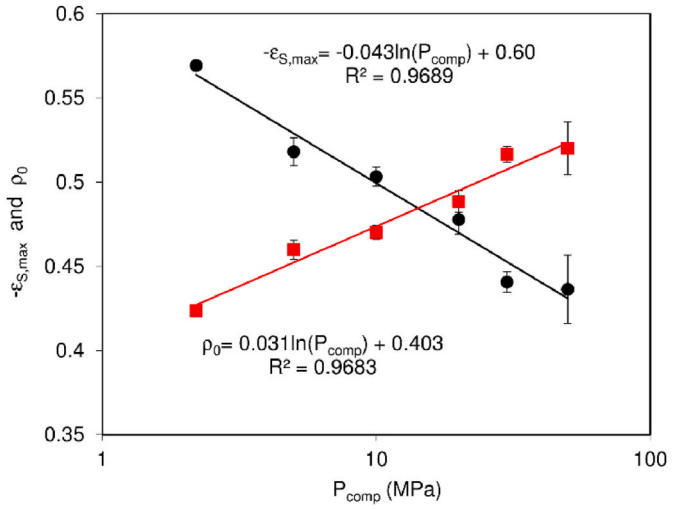

Fig. 15. Evolution of experimental $-\varepsilon_{S,max}$ and calculated ρ_0 (Eq. (31)) with compaction pressure, P_{comp}. Powder M and β = 15K/min.

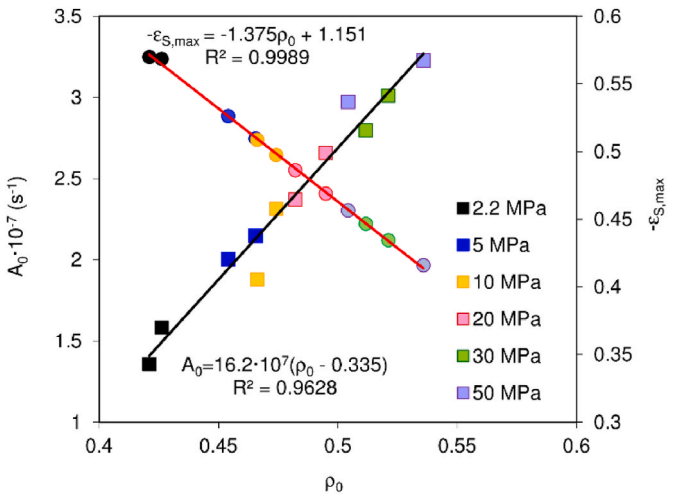

Fig. 16. Evolution of experimental $-\varepsilon_{S,max}$ and calculated A_0 (Eq. (35) with n = 0.7) with calculated initial relative density, ρ_0 (Eq. (31)), at different compaction pressures, P_{comp}. Powder M and β = 15K/min.

3.3.2. *Combined effect of heating rate, β, and powder particle size distribution*

Sintering curves were obtained at different heating rates, β, with each studied particle size distribution (F, M, C, and MC). The values of $-\varepsilon_S$ are plotted versus the corresponding temperatures at 15K/min in Fig. 18.

3.3.2.1. Narrow particle size distributions (F, M, and C). For the narrowest particle size distributions (F, M, and C), the sintering curves exhibited the same shape as the previously studied curves (Figs. 10 and 14), so that they can be described by Eq. (35). Particle size distribution was observed to lower sintering onset and maximum densification temperature, this effect being much greater on going from distribution M to C. It was also verified that decreasing particle size increased maximum firing shrinkage, $\varepsilon_{S,max}$ [44], Table 4 and Fig. 18, owing to decreased relative density at sintering onset, ρ_0, whose values were calculated from Eq. (31) (Table 4). Table 4 also details the values of parameters A_0, κ, and n, obtained by jointly fitting the sintering curves of particle size distributions F, M, and C to Eq. (35), together with the variance, S^2. To calculate the values of A_0 and of κ, first, the values of A were determined by fitting the sintering curves of each PSD to Eq. (25),

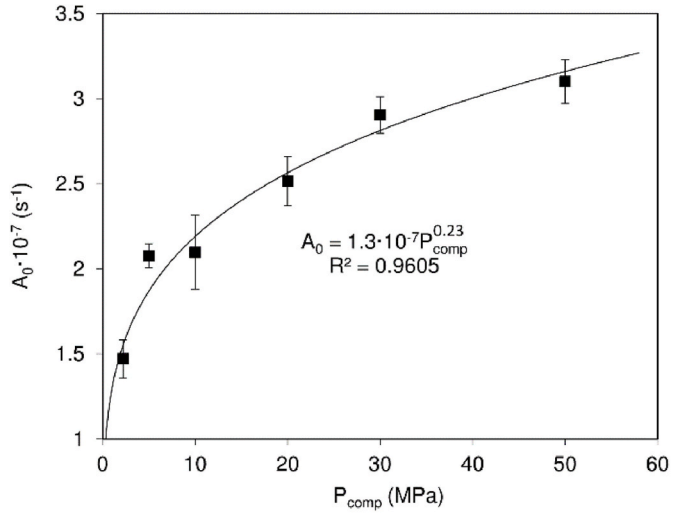

Fig. 17. Evolution of calculated A_0 (Eq. (35) with n = 0.7) with compaction pressure, P_{comp}. Powder M and β = 15K/min.

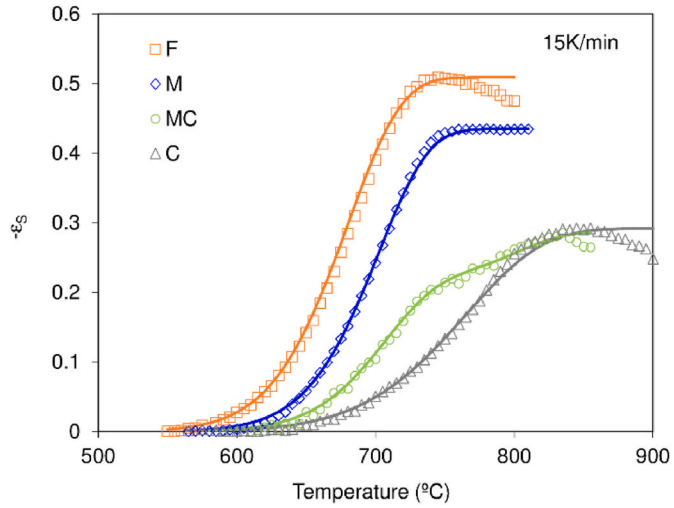

Fig. 18. Evolution of silhouette surface strain, $-\varepsilon_S$, with temperature for powders F, M, C, and MC. β = 15K/min. The symbols are experimental data, and the solid lines correspond to the values calculated from Eq. (35) and parameters in Table 4 for powders F, M, and C and from Eq. (39), Eq. (40), and Eq. (41) and parameters in Table 5 for powder MC.

according to the procedure described in Section 3.2.2. The resulting values of A were fitted to Eq. (34) (Fig. 19) with the following restrictions: a single value of κ and three values of A_0, one for each PSD. The agreement between the experimental and the calculated results was very good (Table 4, Fig. 18, and Fig. 19).

For particle size distributions F and M, which exhibited a very similar sintering range (difference between sintering end and densification onset temperature), the sintering curves could be described by using the same value of n = 0.7. In contrast, the sintering range for particle size distribution C was much larger, so that the value obtained for n was lower (n = 0.58). These results indicate that the relaxation time distribution function was broader for this PSD than for the finer PSDs. This was because sintering onset shrinkage depended on the curvature radius at the interparticle contact points. As the coarsest particles also exhibited sharp edges of small curvature radius (Fig. 5), their sintering onset temperature was lower than expected for their high mean size. As sintering progressed, the particles spheroidised and the interparticle contact area increased, so that the sintering rate in this intermediate stage

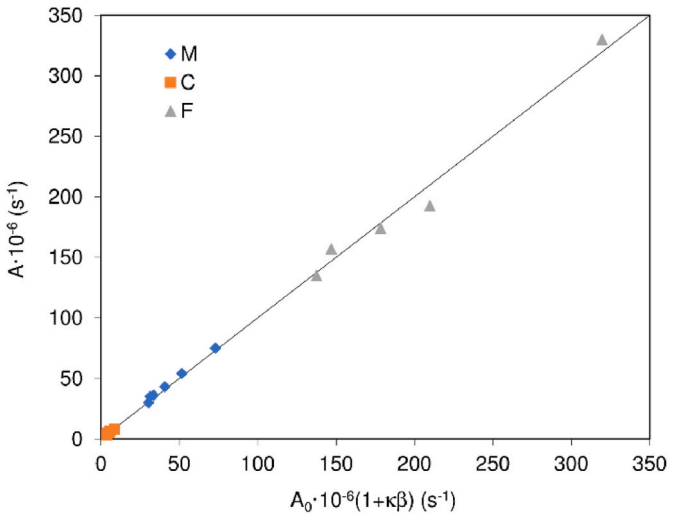

Fig. 19. Comparison of the pre-exponential factor, A, calculated from Eq. (25) with that calculated from Eq. (34), using the values of A_0 and κ in Table 4.

depended much more on mean particle size. In the final stage of the process, in which most porosity was closed, the sintering rate depended on the size of the largest residual pores (with the lowest capillary pressure), whose size depended, in turn, on the size of the coarsest particles. The particle size distribution, albeit not wide, of irregular and coarse particles thus exhibited a broad relaxation time distribution owing, on the one hand, to the presence of sharp edges at the inter-particle contact points, which determined short relaxation times, and on the other to the formation of large-sized pores associated with the coarsest particles, which exhibited long relaxation times.

The value of parameter $\gamma/r\eta_0$ of particle size distributions F, M, and C was calculated from the frit properties and particle mean radius and compared with the corresponding value of A_0 obtained from the fits (Fig. 20). The values of A_0 were about one third the value of the calculated parameters $\gamma/r\eta_0$ (Eq. (37)):

$$A_0 = 0.29 \cdot 10^6 \cdot \left(\frac{\gamma}{r\eta_0}\right) \qquad \text{Eq. 37}$$

Therefore, as had been assumed, pre-exponential factor A of Eq. (22) was related to the process variables by means of equations Eq. (34), Eq. (36), and Eq. (37). That is:

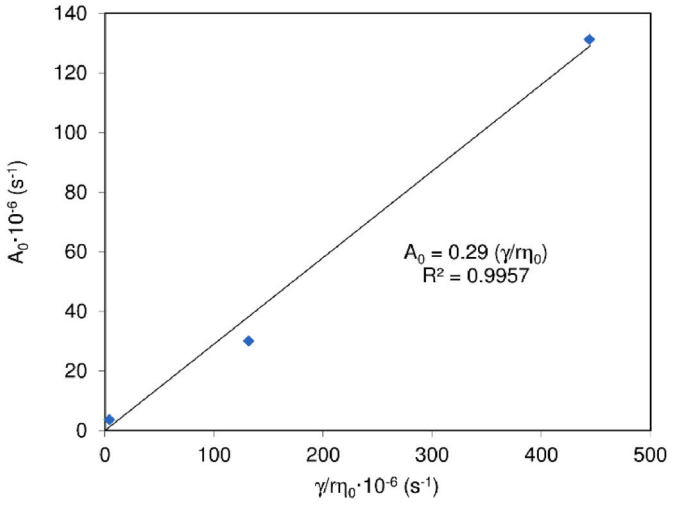

Fig. 20. Relationship between A_0 (Table 4) and $(\gamma/r\eta_0)$ for powders F, M, and C.

$$A \propto (1+\kappa\beta)[a \cdot (\rho_0 - b)]\left(\frac{\gamma}{r\eta_0}\right) \qquad \text{Eq. 38}$$

where a and b are constants.

The first factor takes into account the effect of heating rate on the uniformity of the real temperature of the sample. The second describes the influence of green bulk density on the microstructure of the green compact (compactness, pore size distribution, and number and nature of interparticle contacts). The last term expresses the effect of frit properties and mean particle size.

3.3.2.2. Wide particle size distribution (MC). The sintering curve of the widest particle size distribution (MC) was more complex and therefore required a different mathematical treatment. Indeed, the sintering curve (Fig. 18) was made up of two sections. The temperature range of the first was similar to that of particle size distribution M. In contrast, the behaviour at the end of sintering was very similar to that exhibited by the coarsest particle size distribution (C). The curve suggested that sintering of the MC particle size distribution took place in two differentiated stages, each of which could be described, in principle, by the developed model (Fig. 21). In the first stage, test piece densification stemmed from sintering of the small and medium-sized particles that surrounded the largest particles, thus reducing the separation of the largest particles. As a result, this process exhibited a relaxation time distribution similar to that of particle size distribution M. The other small and medium-sized particles located in the voids formed by the largest particles did not contribute, on sintering, to compact densification but led to formation of large pores. These pores between the largest particles were eliminated in the second sintering stage and pore removal was therefore similar to that in final sintering of particle size distribution C particles (the coarsest). As a result, relaxation time distribution in the second stage, which mainly involved removal of large pores, must be narrower (n_2 of MC must be greater than n of C) and shifted towards long times. In light of this, a model was developed based on the following considerations: i) the degree of sintering progress, α, is the sum of the progress made in the first stage, α_1, and in the second stage, α_2:

$$\alpha = \alpha_1 + \alpha_2 \qquad \text{Eq. 39}$$

ii) The degree of progress in each stage, α_1 and α_2, can be described by the developed relaxation model (Eq. (35)), multiplying each degree of progress by the fraction of one in which it contributes to the overall

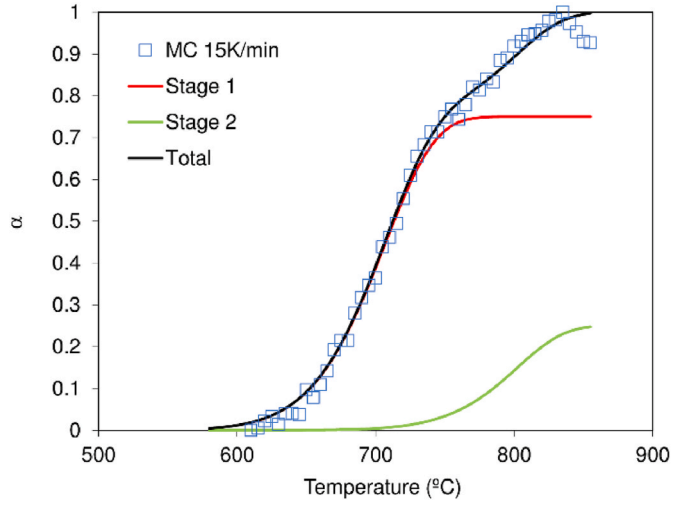

Fig. 21. Sintering curve for powder MC at 15K/min. The symbols are experimental data, and the solid lines correspond to the values calculated from the model: stage 1 (Eq. (40)), stage 2 (Eq. (41)), and total (Eq. (39)), with the parameters from Table 5.

process, w_1 and w_2:

$$\alpha_1 = w_1\left\{1 - exp\left\{-\left[\frac{A_{01}\cdot(1+\kappa\beta)}{\beta}\frac{(T-T_{VFT})^2}{B}exp\left(-\frac{B}{(T-T_{VFT})}\right)\right]^{n_1}\right\}\right\} \quad \text{Eq. 40}$$

$$\alpha_2 = w_2\left\{1 - exp\left\{-\left[\frac{A_{02}\cdot(1+\kappa\beta)}{\beta}\frac{(T-T_{VFT})^2}{B}exp\left(-\frac{B}{(T-T_{VFT})}\right)\right]^{n_2}\right\}\right\} \quad \text{Eq. 41}$$

The five sintering curves obtained at different heating rates, $0.5 \leq \beta \leq 60$ K/min, were jointly fitted to Eq. (39), Eq. (40), and Eq. (41). Table 5 details the values of A_{01}, A_{02}, κ, n_1, and n_2, together with the fit variance, S^2. The first stage contributed more to the sintering process than the second stage, exhibiting a value of $w_1 = 0.75$ and a value of $n_1 = 0.7$, the latter being identical to that obtained for particle size distributions M and F. The second stage exhibited a value of $n_2 = 1$, indicating a very narrow relaxation time distribution, theoretically a single value.

Using the values of A_{01} and A_{02}, taking into account the relationship between this parameter and particle mean radius, r, obtained for the narrowest PSDs (Eq. (37)), the particle sizes corresponding to each stage were estimated (Table 5 and Fig. 20). It was observed that r_1 practically coincided with the mean radius of particle size distribution M, while r_2 was similar to that of particle size distribution C. These results confirmed the validity of the developed model.

4. Conclusions

The sintering of compacts of frit particles with a similar particle size distribution to that used in industrial practice for producing glazes was studied by isothermal experiments (at six temperatures) and six constant heating rates in a hot stage microscope. The results fitted very well to their respective kinetic equations whose development was based on the following assumptions: i) Densification in a gaseous environment leads to minimum residual porosity. ii) For an ordered packing of identical spherical particles, the rate at which this system approaches equilibrium (minimum porosity) is given by the De Donder equation, with a relaxation time that is inversely proportional to glass surface tension and proportional to glass viscosity and to particle radius. iii) For real compacts of irregular particles, the densification rate is a complex relaxation process, with a relaxation time distribution given by the Kohlrausch–Williams–Watts (KWW) equation. iv) The effect of temperature on the sintering rate is given by the effect of temperature on the inverse of glass viscosity.

It was verified, in constant-rate heating experiments, that the pre-exponential factor of the rate constant depended slightly on the heating rate.

It was determined, by constant-rate heating experiments, that raising pressing pressure decreased maximum linear shrinkage and slightly increased the sintering rate, as the pre-exponential factor of the rate constant increased (or relaxation time decreased). In contrast, the stretching parameter remained constant.

The combined effect of the heating rate and particle size distribution of the frit particles was determined by constant-rate heating experiments. For the three particle size distributions with relatively narrow particle size distributions, all used in industrial practice for glaze production, the results fitted very well to the developed equation. For the finest particle size distributions, the values of the stretching factor remained constant, whereas they decreased for the coarsest particle size distribution. In contrast, the pre-exponential factor of the rate constant (or inverse of relaxation time) increased proportionally with the inverse of particle radius. For the much wider particle size distribution than those customarily used in industrial practice, the sintering curve was described as the sum of two stages, each of which was described by the developed model. The first stage described sintering due to the smallest particles, which exhibited a short relaxation time distribution, whereas the second stage was due to the removal of large pores associated with the largest particles, which exhibited a longer relaxation time distribution.

Generally, it was found, by constant-rate heating experiments, that the pre-exponential factor of the rate constant or inverse of relaxation time was proportional: to a linear function of the heating rate, to a power law function of pressing pressure, and to the ratio of glass surface tension to the product, pre-exponential factor of glass viscosity and particle mean radius.

Declaration of competing interest

The authors declare that they have no known competing financial interests or personal relationships that could have appeared to influence the work reported in this paper.

Acknowledgements

This study was co-funded by the Valencia Region Government through the Valencian Institute for Business Competitiveness (IVACE).

References

[1] E.M. Rabinovich, Preparation of glass by sintering, J. Sci. Mater. 20 (1985) 4259–4297.
[2] R. Müller, S. Reinsch, Viscous phase silicate processing, in: N. Bansal, A. R. Boccaccini (Eds.), Processing Approaches for Ceramics and Composites, John Wiley & Sons, Hoboken, New Jersey, USA, 2012, pp. 75–144.
[3] J.L. Amorós, E. Blasco, A. Moreno, E. Zumaquero, C. Feliu, Non-isothermal sintering of powdered vitrified composites. A kinetic model, Mater. Lett. 236 (2019) 236–239, https://doi.org/10.1016/j.matlet.2018.10.089.
[4] J.L. Amorós, E. Blasco, A. Moreno, N. Marín, C. Feliu, Sinter-crystallisation kinetics of a SiO2-Al2O3-CaO-MgO-SrO glass-ceramic glaze, J. Non-Cryst. Solids 532 (2020) 119900, https://doi.org/10.1016/j.jnoncrysol.2020.119900.
[5] J.L. Amorós, E. Blasco, A. Moreno, N. Marín, C. Feliu, Effect of particle size distribution on the sinter-crystallisation kinetics of a SiO2-Al2O3-CaO-MgO-SrO glass-ceramic glaze, J. Non-Cryst. Solids 542 (2020) 120148, https://doi.org/10.1016/j.jnoncrysol.2020.120148.
[6] J. Frenkel, Viscous flow of crystalline bodies under the action of surface tension, J. Phys (USSR) 9 (5) (1945) 385–391.
[7] J.K. Mackenzie, R. Shuttleworth, A phenomenological theory of sintering, Proc. Phys. Soc., London 62 (1949) 833–852.
[8] F.B. Wadsworth, J. Vasseur, E.W. Llewellin, J. Schauroth, K.J. Dobsom, B. Scheu, D.B. Dingwell, Sintering of viscous droplets under surface tension, Proc. Math. Phys. Eng. Sci. 472 (2188) (2016) 20150780, https://doi.org/10.1098/rspa.2015.0780.
[9] J.I. Martínez-Herrera, J.J. Derby, Viscous sintering of spherical particles via finite element analysis, J. Am. Ceram. Soc. 78 (3) (1995) 645–649.
[10] A. Jagota, P.R. Dawson, Micromechanical modelling of powder compacts—I. Unit problems for sintering and traction induced deformation, Acta Metall. 36 (9) (1988) 2551–2561.
[11] F. Wakai, K. Katsura, S. Kanchika, Y. Shinoda, T. Akatsu, K. Shinagawa, Sintering force behind the viscous sintering of two particles, Acta Mater. 109 (2016) 292–299.
[12] Y.M. Chiang, D.P. Birnie, W.D. Kingery, Physical Ceramics, John Wiley, New York, 1997.
[13] M. Prado, E. Dutra Zanotto, R. Müller, Model for sintering polydispersed glass particles, J. Non-Cryst. Solids 279 (2) (2001) 169–178.
[14] F. Wakai, O. Guillon, Evaluation of sintering stress from 3-D visualization of microstructure: case study of glass films sintered by viscous flow and imaged by X-ray microtomography, Acta Mater. 66 (2014) 54–62.
[15] G. Okuma, D. Kadowaki, T. Hondo, S. Tanaka, F. Wakai, Interface topology for distinguishing stages of sintering, Sci. Rep. 7 (2017) 11106.
[16] R.K. Bordia, G.W. Scherer, On constrained sintering — I. Constitutive model for a sintering body, Acta Metall. 36 (1988) 2393–2397.
[17] E.A. Olevsky, Theory of sintering: from discrete to continuum, Mater. Sci. Eng. R. 23 (1998) 41–100.
[18] V.V. Skorohod, Rheological Basis of the Theory of Sintering, Naukova Dumka, Kiev, 1972.
[19] M.N. Rahaman, L.C. De Jonghe, G.W. Scherer, R.J. Brook, Creep and densification during sintering of glass powder compacts, J. Am. Ceram. Soc. 70 (1987) 766–774.
[20] V.M. Sura, P.C. Panda, Viscosity of porous glasses, J. Am. Ceram. Soc. 73 (1990) 2697–2701.
[21] G.W. Scherer, Sintering inhomogeneous glasses: application to optical waveguides, J. Non-Cryst. Solids 34 (1979) 239–256.

[22] J.K. Mackenzie, Elastic constants of a solid containing spherical holes, Proc. Phys. Soc. B 63 (1950) 2–11.
[23] V.C. Ducamp, R. Raj, Shear and densification of glass powder compacts, J. Am. Ceram. Soc. 72 (5) (1989) 789–804.
[24] G. Okuma, D. Kadowaki, T. Hondo, A. Sato, S. Tanaka, F. Wakai, Computation of sintering stress and bulk viscosity from microtomographic images in viscous sintering of glass particles, J. Am. Ceram. Soc. 100 (2017) 867–875.
[25] A. Lukichev, Physical meaning of the stretched exponential Kohlrausch function, Phys. Lett. A 383 (2019) 2983–2987.
[26] J.H. Wu, Q. Jia, The heterogeneous energy landscape expression of KWW relaxation, Sci. Rep. 6 (2016) 20506.
[27] S.L. Shamblin, B.C. Hancock, Y. Dupuis, M.J. Pikal, Interpretation of relaxation time constants for amorphous pharmaceutical systems, J. Pharm. Sci. 89 (3) (2000) 417–427.
[28] N. Rabiei, S.H. Amirshahi, M.H. Kish, Description of physical aging kinetics of glassy polymers by interpretation of parameters of the Kohlrausch-Williams-Watts relaxation function via simulation, Phys. Rev. E 99 (2019), 032502.
[29] T. de Donder, P. van Rysselberghe, Thermodynamic Theory of Affinity: a Book of Principles, Stanford University Press and Oxford University Press, Oxford, 1936.
[30] I. Gutzow, J. Schmelzer, The Vitreous State: Thermodynamics, Structure, Rheology and Crystallization, Springer Verlag Berlin, New York, 1995.
[31] I. Gutzow, Ts Grigorova, I. Avramov, J.W.P. Schmelzer, Generic phenomenology of vitrification and relaxation and the Kohlrausch and Maxwell equations, Phys. Chem. Glasses 43C (2002) 477–486.
[32] E. Blasco, Sinterización de compactos de vidrio y composites vidrio-circón. Mecanismo y cinética del proceso, Castellón (Spain): PhD Dissertation, Universitat Jaume I. Department of Chemical Engineering, 2017.
[33] P. Murray, J. White, Kinetics of the thermal dehydration of clays. Part IV. Interpretation of the differential thermal analysis of the clay minerals, Trans. Br. Ceram. Soc. 54 (1995) 204–264.
[34] T. Ozawa, Kinetics of non-isothermal crystallization, Polymer 12 (3) (1971) 150–158.
[35] National Institute of Standards and Technology. Certificate Standard Reference Material 717a Borosilicate Glass.
[36] J.L. Amorós, A. Moreno, E. Blasco, J.J. Pérez, S. Navarro, S. Reverter, Inkjet technology for ceramic products. Influence of some process variables on ink penetration, Int. J. Appl. Ceram. Technol. 16 (2019) 2153–2160, https://doi.org/10.1111/ijac.13342.
[37] J.M. Fernández-Navarro, El Vidrio, CSIC, Madrid, 1991.
[38] H. Scholze, Influence of viscosity and surface tension on hot stage microscopy measurements on glasses, Ber. Dtsch. Keram. Ges. 391 (1962) 63–68.
[39] M.J. Pascual, L. Pascual, A. Duran, Determination of the viscosity–temperature curve for glasses on the basis of fixed viscosity points determined by hot stage microscopy, Phys. Chem. Glasses: Eur. J. Glass Sci. Technol. Part B 42 (1) (2001) 61–66.
[40] M.J. Pascual, A. Duran, M.O. Prado, A new method for determining fixed viscosity points of glasses, Phys. Chem. Glasses 46 (5) (2005) 512–520.
[41] J.L. Amorós, E. Blasco, Transmisión de calor en la industria cerámica, Valencia Region Government through the Valencian Institute for Business Competitiveness (IVACE), Castellón (Spain), 2019.
[42] J.L. Amorós, A. Escardino, V. Beltrán, J.E. Enrique, Quality control in tile production, Interceram 33 (2) (1984) 50–54.
[43] V. Bagan, Efecto de las condiciones de operación en las diferentes etapas del proceso sobre las propiedades y características de un pavimento de muy baja porosidad, Castellón (Spain): PhD Dissertation, Universitat Jaume I. Department of Chemical Engineering, 1991.
[44] J.L. Amorós, E. Blasco, C. Feliu, A. Moreno, Effect of particle size distribution on the evolution of porous, microstructural, and dimensional characteristics during sinter-crystallisation of a glass-ceramic glaze, J. Non-Cryst. Solids 572 (2021) 121093, https://doi.org/10.1016/j.jnoncrysol.2021.121093.